



Physicochemical and computational insight of ^{19}F NMR and emission properties of meso -(o -aryl)-BODIPYs

Mónica Farfán-Paredes, Oscar González-Antonio, Diana E Tahuilan-Anguiano, Jorge Peón, Armando Ariza, Pascal G. Lacroix, Rosa Santillan, Norberto Farfán

► To cite this version:

Mónica Farfán-Paredes, Oscar González-Antonio, Diana E Tahuilan-Anguiano, Jorge Peón, Armando Ariza, et al.. Physicochemical and computational insight of ^{19}F NMR and emission properties of meso -(o -aryl)-BODIPYs. New Journal of Chemistry, 2020, 44 (45), pp.19459-19471. 10.1039/D0NJ02576C . hal-03150783

HAL Id: hal-03150783

<https://hal.science/hal-03150783>

Submitted on 24 Feb 2021

HAL is a multi-disciplinary open access archive for the deposit and dissemination of scientific research documents, whether they are published or not. The documents may come from teaching and research institutions in France or abroad, or from public or private research centers.

L'archive ouverte pluridisciplinaire **HAL**, est destinée au dépôt et à la diffusion de documents scientifiques de niveau recherche, publiés ou non, émanant des établissements d'enseignement et de recherche français ou étrangers, des laboratoires publics ou privés.

ARTICLE

Physicochemical and computational insight of ^{19}F NMR and emission properties of meso-(o-aryl)-BODIPYs

Received 00th January 20xx,
Accepted 00th January 20xx

DOI: 10.1039/x0xx00000x

Mónica Farfán-Paredes,^a Oscar González-Antonio,^a Diana E. Tahuilan-Anguiano,^a Jorge Peón,^b Armando Ariza,^c Pascal G. Lacroix,^d Rosa Santillan,^c Norberto Farfán^{a*}

A series of electronic and physicochemical parameters were explored to determine their effect on experimental spectroscopic and photophysical data. Through a systematic obtention of a series of *meso*-(*o*-aryl)-BODIPYs, ^{19}F NMR spectra were analyzed and their fluorescence quantum yields in several solvents were measured. Experimental values of ^{19}F chemical shift difference $\Delta\delta_{\text{F}}$ correlate well with σ -Hammett constants, which is indicative of the inductive nature of the functional groups on the fluorine atoms. A computational DFT exploration of rotational energy barriers, electrostatic potential maps, group electronegativity, charge partitions and hardness/softness, provided insight on how those traits can be directly related to the measured features. Expanded understanding of such characteristics provides design arguments and a structure-property relationship, which in a more advantageous way, would help to understand the properties of the synthesized molecules and of future attempts that are structurally related.

Introduction

The family of 4,4-difluoro-4-bora-3a,4a-diaza-s-indacene derivatives, also known as BODIPYs, are strongly UV-absorbing small molecules that emit relatively sharp fluorescence peaks.¹ These compounds are versatile dyes of considerable interest owing to their photochemical stability, synthetic versatility and good solubility in common organic solvents. Moreover, they show large extinction coefficients and tunable quantum yields.^{2–5} For these properties, BODIPY-based dyes have been exploited as fluorescent probes,⁶ molecular sensors,⁷ semiconducting materials,^{8–10} biological labelling,¹¹ viscosity probes¹² and photosensitizers in photodynamic therapy.¹³ Another advantage is that it is possible to tune their spectroscopic and photophysical properties functionalizing adequately any position at the core including boron substituents.¹⁴

The BODIPY core has two pyrrole rings fused with a bridging carbon known as the 8 position or *meso* position and a BF_2 unit

closing a third ring. The structure is co-planar with the electronic density distributed between three rings, while the two fluorine atoms are in a perpendicular plane.¹⁵ Another characteristic of BODIPY dyes related to their photophysical properties is intramolecular rotation. The derivatives with a phenyl ring at *meso* position have freedom of movement and are considerably less fluorescent in comparison with bulky substituents which have restricted movement.¹⁶ A wide variety of groups have been introduced at the *meso* position of the BODIPY core in order to study their influence over the photophysical properties,¹⁷ however, the influence of substituents over fluorine atoms have rarely been studied.¹⁸

In this work, different substituents were introduced at the *ortho*-position of the *meso*-phenyl moiety in order to study their influence over fluorine atoms by ^{19}F NMR as well as its photophysical properties in different solvents. Computational analyses for electrostatic interactions, hardness/softness and dipole moment were carried out and compared with experimental spectroscopic and photophysical results. Furthermore, the relationship between ^{19}F chemical shifts difference $\Delta\delta_{\text{F}}$ of the BODIPY derivatives with the group electronegativity and the σ -Hammett coefficients were investigated.

Results and Discussion

Synthesis and NMR characterization

^a Facultad de Química, Departamento de Química Orgánica, Universidad Nacional Autónoma de México, 04510 CDMX, México. E-mail: norberto.farfán@gmail.com

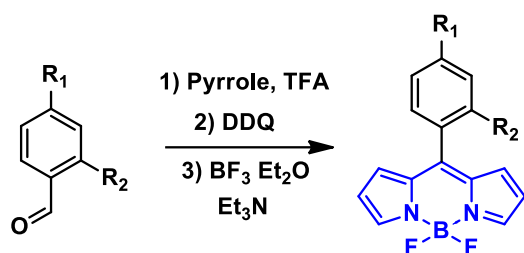
^b Instituto de Química, Universidad Nacional Autónoma de México, 04510 CDMX, México.

^c Departamento de Química, Centro de Investigación y de Estudios Avanzados del IPN, México D.F. 07000, A.P. 14-740, México

^d CNRS, Laboratoire de Chimie de Coordination (LCC), 205 route de Narbonne, BP44099, 31077 Toulouse Cedex 4, France

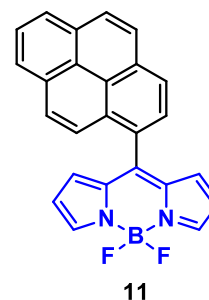
Electronic Supplementary Information (ESI) available: NMR spectra and computational details. See DOI: 10.1039/x0xx00000x

BODIPYs **1–11** were synthesized using the sequence of reactions depicted in Scheme 1. BODIPYs **1–3** were prepared to compare with those that have *ortho*-substituents at the phenyl moiety.



Additionally, a BODIPY with a bulky group (pyrene) **11** was also synthesized. All compounds were characterized by ^1H and ^{13}C ,

- 1 $\text{R}_1 = \text{H}, \text{R}_2 = \text{H}$
- 2 $\text{R}_1 = \text{OMe}, \text{R}_2 = \text{H}$
- 3 $\text{R}_1 = \text{OH}, \text{R}_2 = \text{H}$
- 4 $\text{R}_1 = \text{H}, \text{R}_2 = \text{Me}$
- 5 $\text{R}_1 = \text{H}, \text{R}_2 = \text{OMe}$
- 6 $\text{R}_1 = \text{OMe}, \text{R}_2 = \text{OMe}$
- 7 $\text{R}_1 = \text{H}, \text{R}_2 = \text{OH}$
- 8 $\text{R}_1 = \text{H}, \text{R}_2 = \text{Cl}$
- 9 $\text{R}_1 = \text{H}, \text{R}_2 = \text{F}$
- 10 $\text{R}_1 = \text{H}, \text{R}_2 = \text{NO}_2$
- 11 Pyrenyl



Scheme 1. General procedure for synthesis of BODIPY derivatives **1–11**.

^{11}B and ^{19}F NMR which provided valuable information concerning the symmetry of the molecule.

Compounds **1–3** showed a typical triplet signal in ^{11}B NMR and a characteristic quartet in ^{19}F NMR due to ^{11}B - ^{19}F couplings $^1J_{\text{B,F}} = 28$ Hz, which is in accordance with the literature.¹⁹ The ^{19}F NMR spectra for these compounds showed that there is a symmetry plane in the molecule and therefore fluorine atoms are equivalent. The introduction of *ortho* substituents at the phenyl moiety or a bulky group like pyrene restricts the freedom of movement at the *meso* position and therefore the chemical environment for each fluorine atom is different, as evidenced in ^{19}F NMR.

A similar example was reported for a BODIPY having a phenanthrene unit at the *meso*-position.¹⁸ The ^{19}F NMR spectra of BODIPYs **4–11** showed a doublet of quartets for each fluorine atom due to ^{19}F , ^{19}F coupling (doublet) and ^{19}F , ^{11}B coupling (quartet). As might be expected, the chemical shift difference between the fluorine atoms ($\Delta\delta_{\text{F}}$) varies with the substituent (Fig. 1).

The chemical shift is dependent on the electronical environment that surrounds an atom, thus, the fluorine atom in the opposite side of the *ortho*-substituent is de-shielded and appears to high frequency, while the fluorine atom in the same side of the *ortho*-substituent is shielded and its signal appears to low frequency. The ^{11}B -decoupled ^{19}F NMR spectra denoted as $^{19}\text{F}\{^{11}\text{B}\}$ were also recorded showing a single signal at -145.18 ppm for BODIPY **2** with a -OMe group at the *para* position (Fig. 2a). On the other hand, BODIPY **5** with the -OMe group at the *ortho* position of the phenyl moiety appears as an AB signal (Fig. 2b).

The $^{19}\text{F}\{^{11}\text{B}\}$ spectrum of **5** showed a doublet corresponding to one of the fluorine atoms at -144.5 ppm (denoted as F_a) and a doublet for the second fluorine atom (denoted as F_b) at -145.6 ppm with a chemical shift difference of 1.1 ppm and a coupling constant ^{19}F , ^{19}F of $^2J_{\text{F}_\text{a},\text{F}_\text{b}} = 107$ Hz.

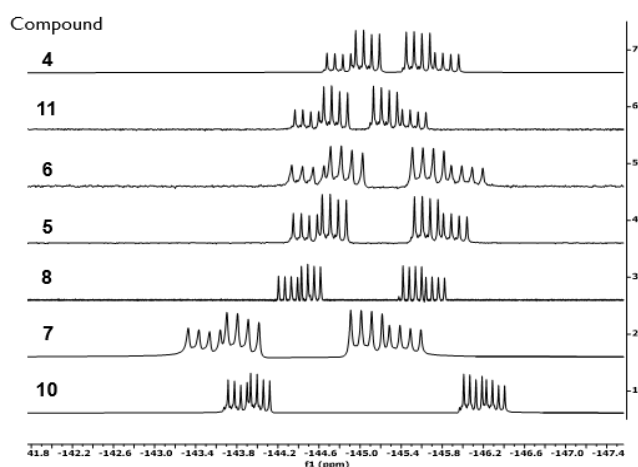


Fig. 1. Stacked ^{19}F NMR spectra of compounds **4–11**. Spectra were stacked from smallest to largest chemical shift difference ($\Delta\delta_{\text{F}}$).

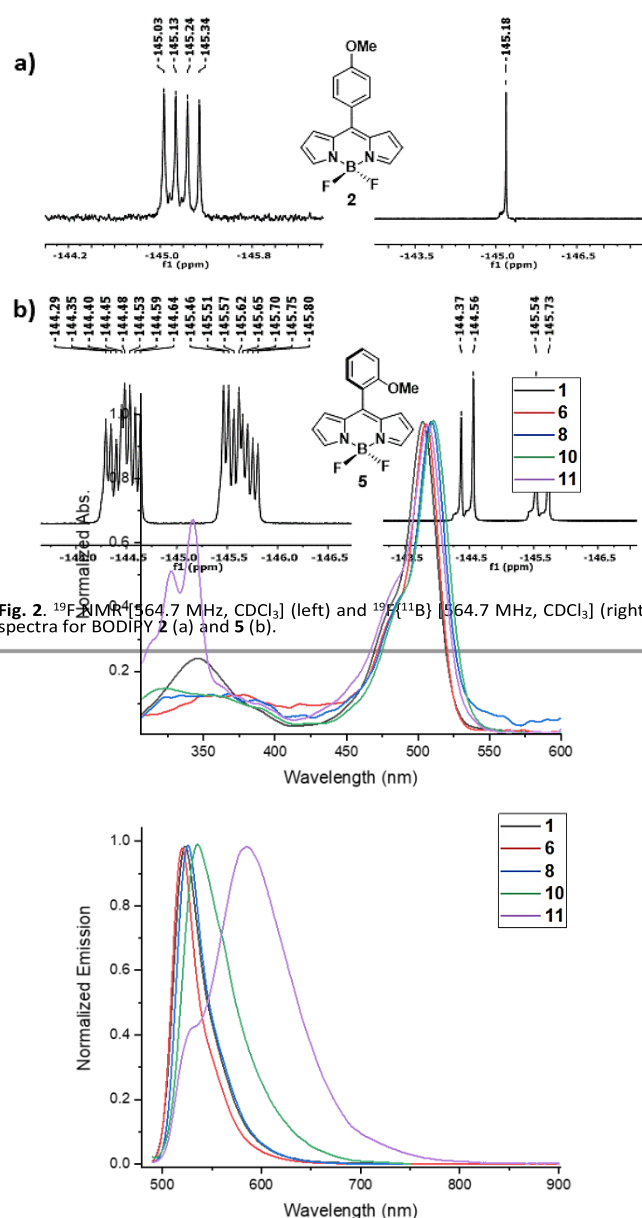
Compound	δ_{Fa}	δ_{Fb}	$\Delta\delta$	$J_{Fa,Fb}$ [Hz]	δ_B	$J_{B,F}$ [Hz]
4	-144.87	-145.56	0.69	107	0.31	29
5	-144.47	-145.63	1.16	107	0.30	29
6	-144.56	-145.72	1.16	107	0.29	29
7	-143.72	-144.94	1.22	104	-0.28	28
8	-144.47	-145.67	1.20	107	-0.69	28
9	-143.88	-145.35	1.47	107	-	28
10	-143.92	-146.32	2.39	104	-0.70	28
11	-144.51	-145.26	0.74	104	-0.06	28

The fact that the rotation of the -OMe substituted phenyl is hindered leads to fluorine atoms that are not equivalent and this kind of compounds can be used to form atropisomers.²⁰ ^{11}B -decoupled ^{19}F NMR spectra were determined for BODIPYs **4–11** (See supporting information). The obtained chemical shifts and coupling constants of BODIPYs **4–11** are listed in Table 1. Compound **4** with the methyl group in the *ortho* position of the phenyl moiety showed the smallest chemical shift difference ($\Delta\delta_F = 0.69$ ppm), while BODIPY **10** which has a nitro group showed the largest chemical shift difference ($\Delta\delta_F = 2.39$ ppm). The ^{19}F NMR spectra in toluene- d_8 (ESI[†] Fig. S31), determined in the range from 30°C to 90°C, show a 0.6 ppm low-frequency shift but maintained the $\Delta\delta_F$, which means the rotation barrier is > than 16.5 kcal/mol.

Photophysical Properties

Photophysical properties such as absorption maximum ($\lambda_{\text{abs max}}$), emission maximum ($\lambda_{\text{emis max}}$), Stokes shift ($\Delta\bar{\nu}$) and fluorescence quantum yields (Φ_F) were measured in four different solvents (See Supporting Information, Table S1). The normalized absorption and emission spectra of selected BODIPYs in toluene are shown in Fig. 3.

Regardless of the nature of the *meso*-aryl substituent, the BODIPYs show an origin band around 500 nm that corresponds to $S_0 \rightarrow S_1$ (π - π^*) transition which is slightly redshifted in non-polar solvents such as hexane and toluene. The shoulder at lower wavelength is due to the 0 – 1 vibrational transition. The value of the fluorescence quantum yield is much lower in BODIPYs **1–3** (highest value $\Phi_F = 0.11$ for **2** in toluene) compared to BODIPYs **4–11** (highest value $\Phi_F = 1.05$ for BODIPY **4** in toluene, the value greater than one is relative to the standard Rhodamine 6G).²¹ The *ortho* substituents at the phenyl moiety restrict freedom of movement promoting the radiative relaxation pathway. BODIPY **5** with a -OMe group at the *ortho* position has a fluorescence quantum yield four times larger ($\Phi_F = 0.20$) than BODIPY **2** with the -OMe group at the *para* position ($\Phi_F = 0.05$) in hexane. BODIPY **10** with the nitro group showed the smallest values ($\Phi_F = 0.01$ or less) due to their highly efficient intersystem crossing that quenches the fluorescence.²² The fluorescence spectra are strongly dependent on the polarity of the solvent. Thus, the fluorescence quantum yields are quenched in polar solvents due to electron transfer process.²³



Geometry optimizations yielded the global energy minima for the studied BODIPY derivatives, which helped determine that for all the synthesized aryl-substituted compounds, there is a torsion that yields a pronounced dihedral angle between the well-known planar BODIPY moiety and the *o*-aryl plane. Being both planar portions, that characteristic allows to automatically define the dihedral angle.

For the *meso*-phenyl-BODIPY **1** whose substituent would be regarded as the reference for the study, that means hydrogen, such dihedral angle (highlighted cyan atoms in Fig. 4) was calculated as 54.9° and is the smallest among all the *ortho*-substituted systems. The rest of the derivatives show values ranging from 60.6° for fluorine up to 117.7° for the pyrenyl-substituted compound.

Fig. 4 gives some examples (compounds **1**, **4**, **7** and **9**) of the calculated structures adding another important feature to the description. The dipole moment vector shows a deviation from the BODIPY plane. This divides the studied species into two sets: the first one includes those derivatives in which the dipole moment vector deviates from the BODIPY plane towards the functional group of interest (H, pyrene, OH and OCH₃ described with a negative angle) and the other set contains those derivatives in which this vector deviates opposite to the location of the highlighted functional group (CH₃, F, Cl and NO₂, described with a positive angle). The remaining compounds can be found within the supporting information (S17-19).

Evaluation of the rotational energy barriers and their influence on the fluorescence quantum yield

Starting from the optimized geometries and the energy minima for *ortho*-substituted species, and the *meso*-(*p*-OMe-phenyl)-BODIPY (**2**) for comparison reasons, the rotational scan provided the torsion angle at which the energy is maximum, and then a transition state TS optimization was carried out to obtain the actual structure for the rotational TS (TS_{rot}) for obtaining the energy of the rotational barrier for each compound.

The complete series of rotational scans (S20) allowed us to divide the studied species in three groups, one group (compounds **1**, **2**, **5**, **7** and **9**) where the dihedral angle for the ground state (GS) conformation was below 90°. For these species, when the systems reach a dihedral angle of 90° this value corresponds to a local maximum during the scan. These local maxima differ only by 2.5 kcal/mol and, therefore, they could be considered conformers in equilibrium. The second group (compounds **4**, **10** and **11**) where the GS conformation possesses a dihedral angle larger than 90° and possess one true maximum at the TS_{rot}. The final is formed only by the chloride-containing species, whose GS conformation has a dihedral angle in the vicinity of 90° and presents no local minimum.

TS_{rot} structures are shown for selected species in Fig. 5, alongside the rotational barriers for all calculated species, the dihedral angle where the energy maximum is reached, and their corresponding fluorescence quantum yield determined experimentally in this work. The calculated structures evidence

that the molecule needs to undergo a deformation from the BODIPY plane in order for the *meso* substituent to rotate. All

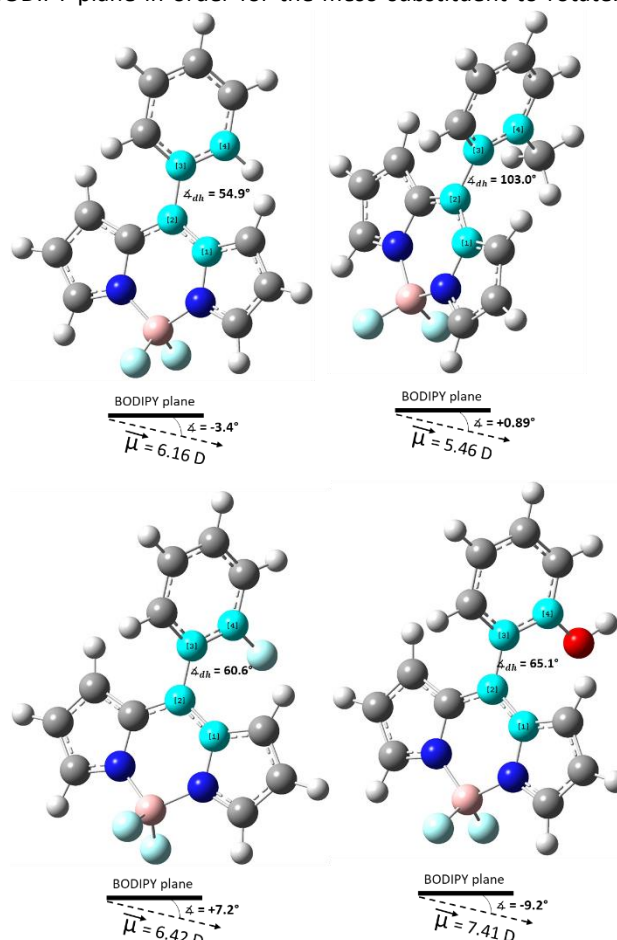


Fig. 4. Dihedral angles and dipole moment vector deviates from the BODIPY plane for compounds **1**, **4**, **7** and **9**.

other TS_{rot} geometries can be found in the Supporting Information (S30).

A detail not to be disregarded, is that for the *o*-hydroxyl group two conformers were studied, as shown in Fig. 6; one where the OH points towards the BODIPY core and another one pointing away from it. Energy differences for both, the optimized energy minima (1.14 kcal/mol) and their corresponding TS_{rot} (0.97 kcal/mol) were small and, therefore, considered as equilibrium conformers. From these results there are several points to be considered.

By plotting the vertical excitations for selected points of the rotational scan and comparing the behavior in energy for both S_0 and S_1 states (the complete series is available from ESI S20 to S29 together with the plots of the oscillator strengths of the corresponding excitations as a function of dihedral angles) we could observe important elements. It is important to note that in all cases, S_1 decreases in energy as the dihedral angle approaches the dihedral angle of maximum energy in the scan, meaning that, as the *meso* substituent attempts the rotation through the BODIPY plane and the conformation requires more energy to be reached, the energy required for the $S_0 \rightarrow S_1$ decreases, making this transition more energetically available. But the energy differences between the rotational barrier and its corresponding vertical excitation vary in three different trends.

The first trend is for the species with known rotation through the BODIPY plane within the conditions and timescales of the performed photophysical studies (reinforced by magnetic equivalent fluorine atoms in the BODIPY core). For such compounds, the energy differences are all bigger greater? than 45 kcal/mol. As can be seen in Fig. 7, compound **2** reaches its rotational barrier at 181° in dihedral angle, still has not reached the lowest value for the vertical transition towards S_1 . This means the phenyl plane rotates through the BODIPY plane first (explaining the equivalence of fluorine atoms in the BODIPY core seen in NMR experiments), and after the phenyl portion rotates through the BODIPY plane, at a dihedral angle of 186° the transition now reaches the lowest point in the curve, having no more geometric hindrance, the molecule can favor the emission process, which explains the enhanced fluorescence quantum yield. This same phenomenon could be observed for the *p*-aminophenyl computed species.

The next visible trend applies for compounds **4**, **5**, **8** and **9**. These species follow the pattern showed in Fig. 7 for *meso*-tolyl-BODIPY, **4**. The vertical excitations reach a minimum right in the point where the TS_{rot} occurs. But for **5** and **9**, the energy difference that goes from the rotational barrier in the electronic GS towards S_1 is larger than for **4** and **8**, whose values are amongst the lowest, providing an explanation for their high quantum yields. Whilst all these species possess larger values of quantum yield, the lower the difference between S_0 (at the TS_{rot} geometry) and S_1 (at the dihedral angle of the TS_{rot} geometry), the larger the quantum yield.

Compounds **7**, **10** and **11** are all particular cases. For the hydroxy-bearing species, as depicted in Fig. 7 the lowest value for the vertical transition $S_0 \rightarrow S_1$ takes place before (dihedral angle of 185°) the TS_{rot} geometry is reached (190°). Which means that the geometry needed for such transition to be most favored is less sterically constrained than the TS_{rot} . The only

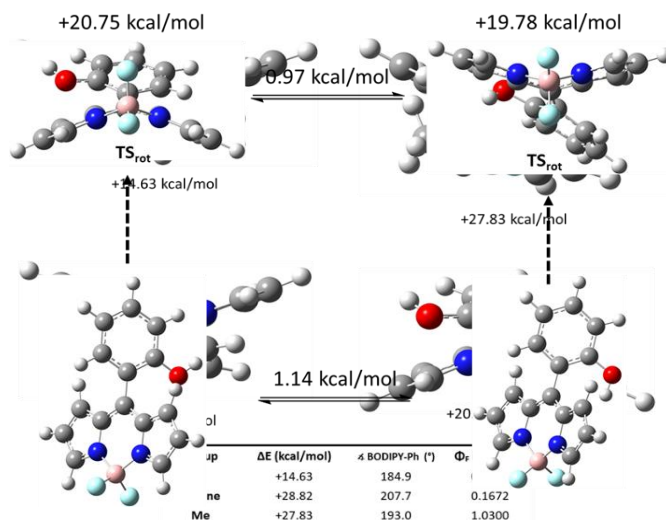


Fig. 6. Calculated hydroxyl-substituted conformers for the study of rotational barriers of compound **7**.

o-OMe	+20.00	191.7	0.2000
NO ₂	+26.08	199.0	0.0100
p-OMe	+25.10	180.9	0.0500

Fig. 5. Geometries for selected TS_{rot} , rotational barriers and dihedral angles to reach the energy maxima for all computed species and fluorescence quantum yields in hexane.

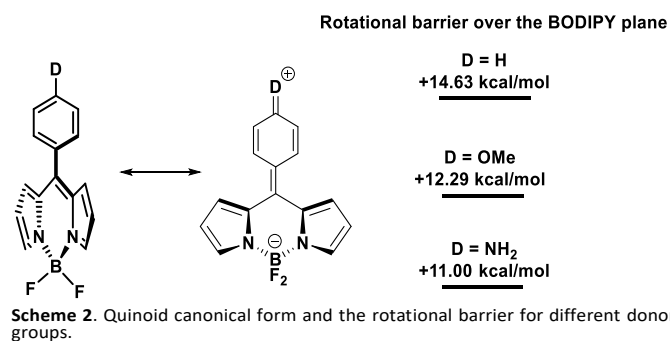
detail is that the vertical excitation energy is higher than in the case of **4** and **8** and this explains the enhanced quantum yield compared to **1**, but not as high as the *meso*-*o*-chlorophenyl and *meso*-tolyl derivatives.

In the case of **10**, the comparison between the rotational scan and the vertical excitation energies towards S_1 , behaves in such a way that the most favored vertical transition occurs at the TS_{rot} geometry and the differences is in the range of the highest emission compounds, which would mean a high quantum yield for nitro-bearing compounds. But, as it is known²² and we have mention before, the highly efficient intersystem crossing of nitro group keeps this compound outside efficiently emitting.

The last case is **11**, where we can observe that there is severe steric restriction, providing the highest rotational barrier, for this compound, the curve of vertical excitations towards S_1 , show the existence of four geometries near TS_{rot} that would provide the most favored vertical excitation and the lowest value occurs before the dihedral angle reaches the geometry for TS_{rot} . This vertical excitation is in the range of compounds **5**, **7** and **9**. It is important to mention that the excited state of the pyrenyl-containing derivative, should possess the largest number of vibrational modes and in spite of having more than a five-fold increase in quantum yield, those vibrational modes give rise to underlying states that hinder the radiative pathways of relaxation from the excited state. The peculiarity observed for *meso*-pyrene-BODIPY is reflected by the behavior of the oscillator strengths of the calculated vertical excitations, being the only species that when reaching the most favored values for the $S_0 \rightarrow S_1$ transition the oscillator strengths increase in for those values of dihedral angle. This means that for those conformations, the orbital overlap of the HOMO-1 \rightarrow LUMO transition is more prominent than for the GS conformation, which could contribute to intermolecular interactions with more *meso*-pyrene-BODIPY molecules or with the solvent that would not be present in any other species.

It is of great importance to mention that the imaginary frequencies for the TS_{rot} are small in magnitude (ranging from -26 cm^{-1} to -73 cm^{-1}) which are not usual for a true TS. This would mean that the potential energy surfaces for electronic GS or excited states would be more complex than what is intuitive²⁶ and they would possess underlying states in general. This complexity would call for more sensitive and more in-depth methodologies that would provide a complete description of dynamics and energetics.

One fact that supports the complexity involved in describing the energetics of these processes is, for example that the barrier for the other computed *para*-substituted compounds (BODIPY **2** and **3** for comparison) shows a decrease in rotational barrier for the *p*-OMe bearing species, but an increase of 66% in quantum yield, which means that for the GS conformation, the rotational process should be even more favored than emission in comparison to the base *meso*-phenyl-BODIPY **1**.



Nonetheless, the electron-donating effect of the *p*-OMe

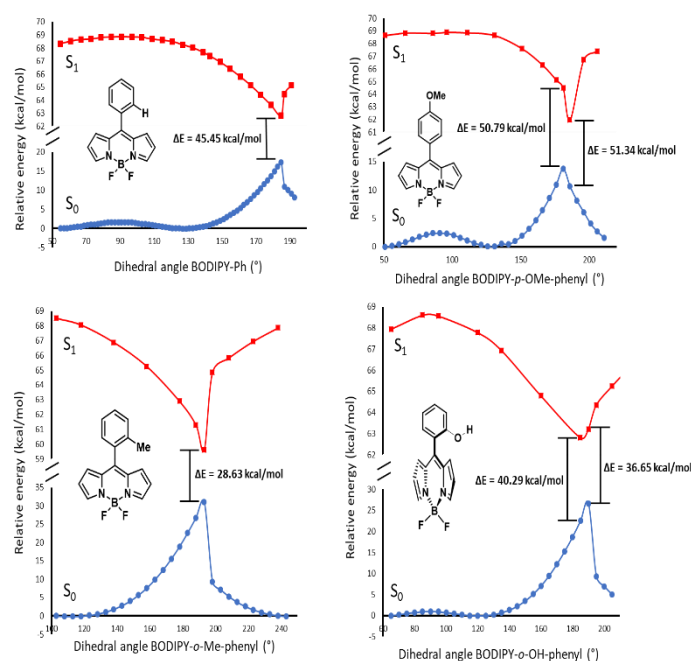


Fig. 7. Selected examples of evolution in energy for the S_1 excited state as a function of the dihedral angle.

substituent is enough to create some push-pull effect from the methoxy group towards the BODIPY. The TS_{rot} geometry and energy for the *p*-NH₂ substituted species show that when the electron-donating effect increases, it causes a decrease in rotational barriers as is shown in (S26). This electronic communication can be explained through the *quinoid* canonical form shown in Scheme 2, which, once in the excited state, should adopt a conformation where rotation is precluded in such a way that a radiative relaxation pathway is preferred, increasing the quantum yield with better electron-donating substituents.

Effect of Electrostatic Features on NMR-Spectroscopic and Photophysical Properties

I. Electrostatic interactions

The computationally obtained structural and physicochemical results show that only the derivatives with *para*-substitution (**1**–**3**) would be energetically allowed to rotate. For the cases in which the *ortho* substituents in the phenyl are energetically locked, an electrostatic and magnetic interaction between the *ortho*-substituents and the nearest fluorine atom gives rise to a difference in chemical shifts ($\Delta\delta_F$), observable in the ¹⁹F NMR spectra. Through a series of computational analyses, we were able to find a series of trends that account for the $\Delta\delta_F$. The first parameter to explore is related to how electrostatic interactions between the fluorine atoms in the BODIPY and the functional group of interest in the phenyl moiety, govern the behavior of $\Delta\delta_F$ which, as we can see in the ESP maps (obtained at an isovalue of 0.002 in Fig. 8), can vary from attractive (in the case of those BODIPY derivatives with small $\Delta\delta_F$), to repulsive for the species with large difference in chemical shift; as if when

the partial charge in the functional group *ortho* to the BODIPY becomes more negative, the interaction with the closest fluorine atom increases the shielding with respect to their magnetic behavior, increasing the value of $\Delta\delta_F$ as well.

The existence of this electrostatic interaction can be further visualized in the contours calculated at an isovalue of 0.002 presented in Fig. 9. These contours were obtained for the plane crossing the main atom in the functional group of interest. It can be seen how for hydrogen, the plane passing through the center of the atom creates level curves indicating the interaction with fluorine, but also with the BODIPY portion of the molecule, and being chemically and electrostatically equivalent for the other *ortho* hydrogen, this leads to equivalent fluorine atoms and no differences in magnetic behavior. For BODIPY **4** with the methyl group, the carbon and hydrogen atoms are interacting almost solely with fluorine for that level curve and is totally differentiable from the interaction for the remaining *ortho* hydrogen.

The fact that there are level curves for the interaction between the methyl and fluorine, and the attractive character of such electrostatic interaction, provides a small but NMR-detectable $\Delta\delta_F$ for the two fluorine atoms. For BODIPY **10** with the nitro substituent, we can observe the particular interaction between the nitro group and the fluorine that produces the $\Delta\delta_F$, and the strongly repulsive character of the interaction sets GIVING? the largest value among the explored series of BODIPY derivatives. Images for the rest of the studied compounds can be found in the Supporting Information (S34–41).

II. Dipole Moment Vectors and Transition Dipole Moments

Let us revisit the values for the deviation angle between the BODIPY plane and the dipole moment vectors shown in Fig. 4 and make a comparison between the angles, the dipole moments of the studied systems, the transition dipole moments for the main excitation of each one of them and their respective values of fluorescence quantum yield (Φ_F).

Calculated dipole moments, the angle regarding the BODIPY plane, and the quantum yield values are given in Table 2. Setting the fluorescence value of 0.03 for the meso-phenyl BODIPY **1** as reference and helped by the rotational barriers studied above, the data shows that, in this case, rotation of the phenyl group is favored over the fluorescence pathway.

As mentioned before, the value for the nitro-containing species decreased threefold, which is typical for nitro-substituted species, since the nitro group quenches fluorescence via intersystem crossing.²² For all other species the quantum yield is higher, in accordance to the restricted non-radiative relaxation pathways upon introduction of the *ortho* substituent in the *meso*-phenyl moiety.²⁶

The Fluorescence quantum yield was plotted as a function of dipole moment vector deviation and transition dipole moment (Table 2 and Fig. 10). Positive angles in the deviation from the BODIPY plane, correspond to the species with the highest quantum yields, whilst all the negative angles are for species

with 0.3 or lower values for this photophysical feature. This

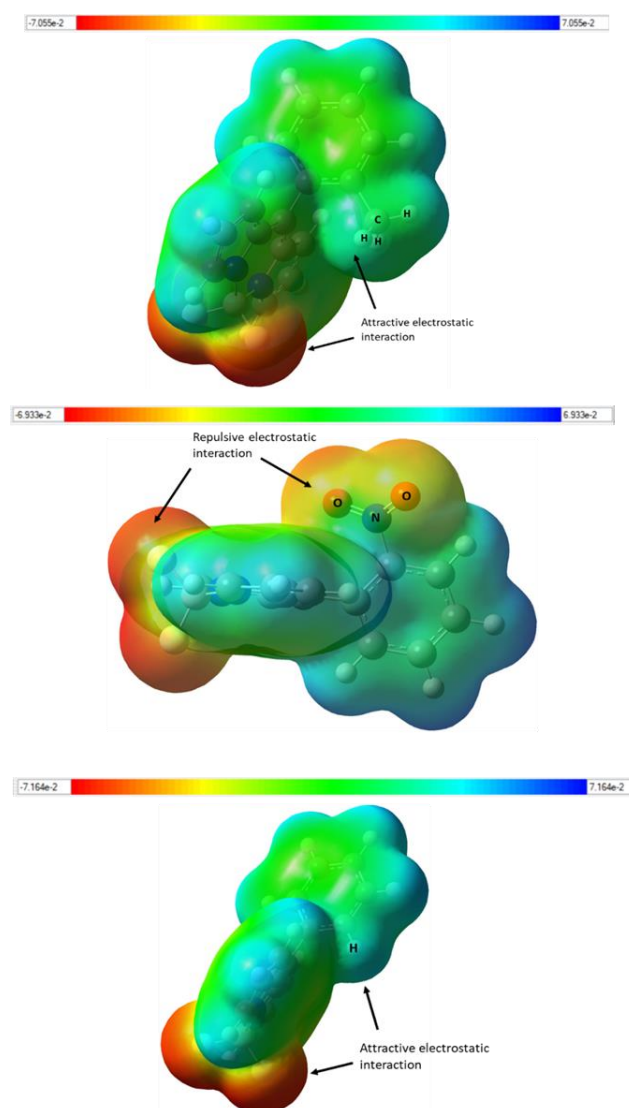


Fig. 8. Electrostatic potential (ESP) maps for some selected species where the difference between attractive and repulsive interactions are observable. Computed with a B3LYP/6-31g(d,p) theory level with a CPCM solvation model in hexane.

creates a valuable design parameter to estimate an interval of quantum yield by calculating the deviation angle thus providing structure-property relationship arguments.

Similarly, three groups can be noticed from the plotted data shown in Fig. 10; the two lowest values (0.01 and 0.03) were explained before, followed by the series of compounds with

increased Φ_F (from 0.16 to 0.31) which correspond to those showing hindered rotation and the low values of transition dipole moment. Finally, the last family of compounds, show a large increase in quantum yield (>0.70) which correspond to hindered rotation and the largest transition dipole moments, leading to a structure-property relationship argument in terms of the behavior of this electronic characteristic.

III. Group electronegativity and Inductive Effects

Having a series of functional groups that share differently the electron density of the phenyl moiety to which they are bonded, gave us a parameter to be considered. Fig. 11 shows how the $\Delta\delta_F$ changes as the group electronegativity²⁷ increases for the *ortho* substituents. Plotting the data, a fairly acceptable correlation can be obtained, showing that the variables are directly proportional. The inductive effect is due to differences in electronegativity between atoms bonded together.

Table 2. Selected data of the different groups.

Compound	Group	Δ BODIPY- μ_{calc} ($^{\circ}$) ^A	μ_{calc} (D) ^A	$S_0 \rightarrow S_1$ μ_{calc} (D) ^B	Φ_F in hexane ^C
1	H	-3.4	6.16	6.66	0.0300
11	Pyrene	-8.70	6.40	6.13	0.1672
4	CH ₃	0.89	5.46	6.87	1.0030
9	F	7.2	6.42	6.76	-
8	Cl	8.5	6.29	7.00	0.7200
7	OH	-9.20	7.41	5.06	0.3100
5	OCH ₃	-15.7	7.19	6.63	0.2000
10	NO ₂	-27.4	7.74	6.21	0.0100

^ACalculated from the geometry optimizations at the B3LYP/def2SVP theory level using the SMD solvation model in hexane

^BCalculated through TD-DFT computations at the B3LYP/6-311g(d,p) theory level using the CPCM solvation model in hexane.

^CObtained experimentally in this work.

Based on the relation between electronegativity and the $\Delta\delta_F$, σ -Hammett coefficients related to inductive effects (σ_i) were also taken into account.²⁸ Fig. 12 shows that $\Delta\delta_F$ increases as the σ -Hammett coefficients increases.

IV. Functional group hardness/softness

Besides the property of attracting electron density as a functional group, it was important to evaluate the effect of that electron density once distributed in the *ortho* substituent. The hardness/softness of phenyl-substituents was calculated using reported values and equations.²⁹ and The results of the NPA we performed, reported as the charge of the *ortho* functional group (Q_G). That information can be consulted in Table S2.

With our data treatment we found that monoatomic substituents such as fluoride and chloride are the hardest, followed closely by hydrogen. In the middle of the interval, one

finds the hydroxyl and methyl groups. Finally, the nitro group,

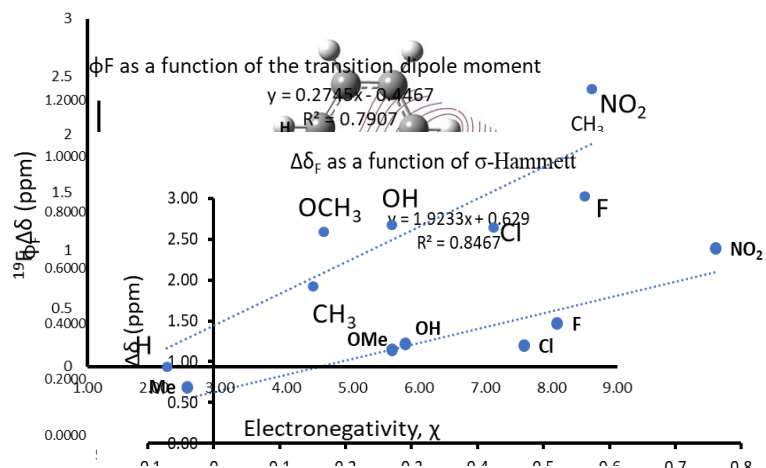


Fig. 11. $\Delta\delta_F$ as a function of group electronegativity. Group electronegativity values were taken from Ref. (28). $\Delta\delta_F$ values were obtained from the ^{19}F NMR spectra determined in the present contribution.

Fig. 12. Linear relationship between $\Delta\delta_F$ and σ_i .

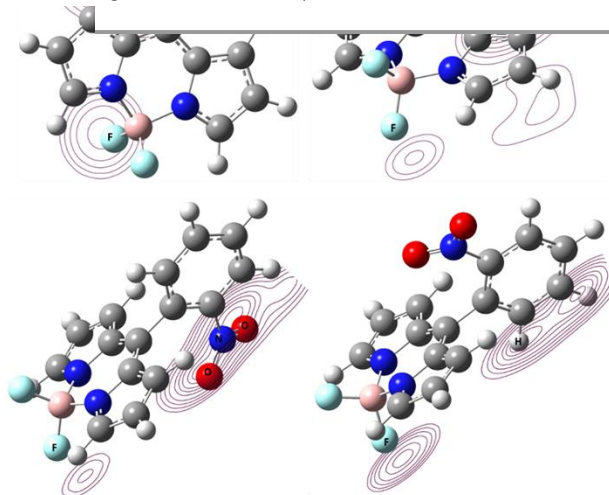


Fig. 9. Level curves for the electrostatic interactions displayed for the plane sectioning the *ortho* substituent. Computed with a B3LYP/6-31g(d,p) theory level with a CPCM solvation model in hexane.

the methoxy and the pyrenyl are prone to be labelled as soft. It is important to keep in mind that not only the charge located on each functional group is relevant to acquire the term soft or hard, but also the thermodynamic properties of ionization potential and electron affinity which are regarded within the Mulliken-Jaffe parameters.

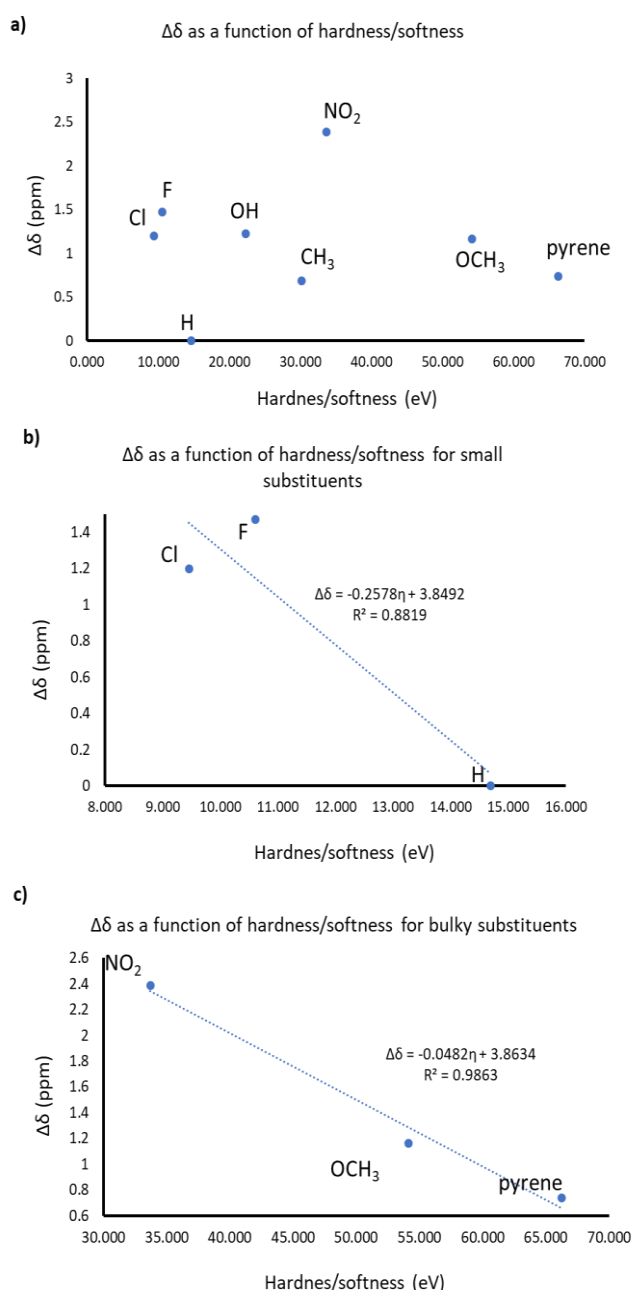


Fig. 13. Plots for the data of $\Delta\delta_F$ vs hardness/softness of the studied *ortho* substituents.

Fig. 13 shows the trends found and the correlations between the hardness and softness of the *ortho* substituents and the $\Delta\delta_F$. Looking at the complete panorama of the plotted values there is no clear correlation, but when the data is divided in sections some information is apparent. For the monoatomic substituents, the hard-functional groups attached to the phenyl moiety, there is a clear correlation where the $\Delta\delta_F$ decreases as hardness decreases, or as softness increases.

The lack of another central point in the data, that may correspond to nitrile, just to provide an example, poses a limitation for claiming a trend or correlation for that section in the plot. In spite of that, there is the third section of the values that also presents a linear, inversely proportional correlation for

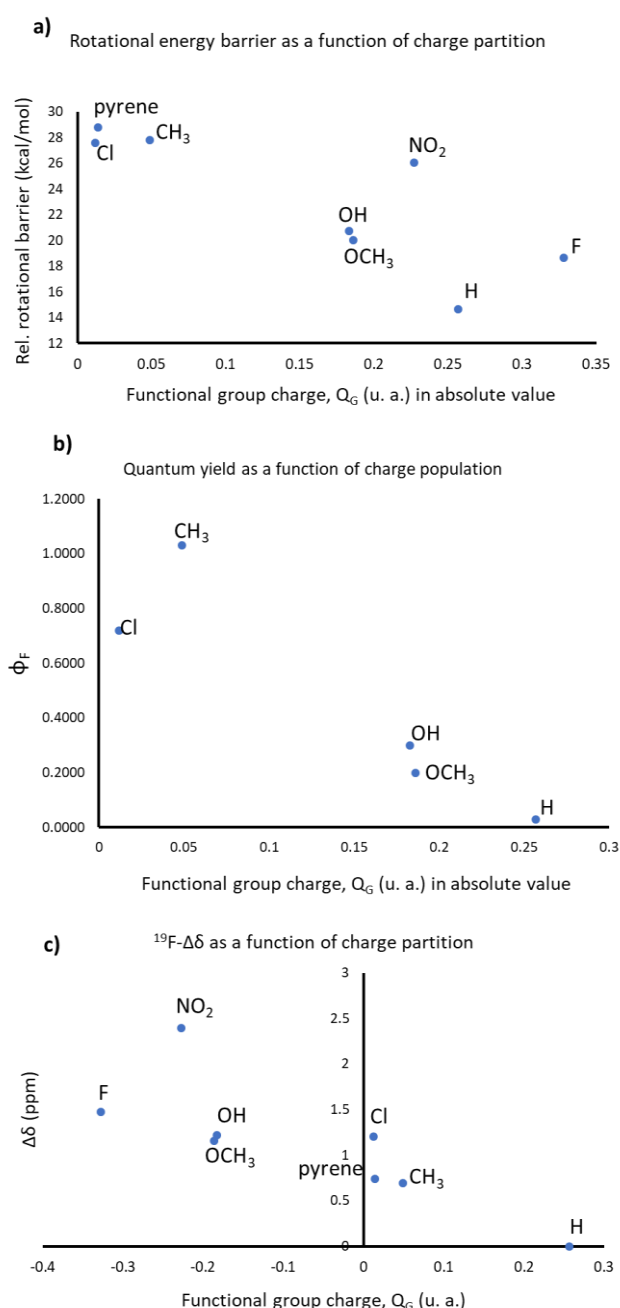


Fig. 14. Trends of rotational energy barrier, fluorescence quantum yield and $\Delta\delta_F$ established by the magnitude of the charge partition of the *ortho*-substituent.

$\Delta\delta_F$ and softness, which would give different linear behavior depending on the bulkyness of the *ortho* substituent.

Finally, a parameter we obtained through NPA charge partition, that brings together all studied and measured features, is the calculated charge for the *ortho*-substituents (Q_G), which establishes a trend with the rotational energy barriers, the $\Delta\delta_F$ and the Φ_F as shown in Fig. 14. For the rotational energy barriers (Fig. 14a) the absolute value of Q_G was used, and by doing this, a clear trend where the *ortho*-substituents with largest charge are the ones with a lower rotational barrier, and as the functional group tends to neutrality, the barrier becomes larger. This same trend is observed for Φ_F . Eliminating two cases: nitro

for its low fluorescence for reasons discussed above, and pyrenyl because of the nuances of the exceeding amount of vibrational relaxation modes. Fig. 14b shows, that as the absolute value of Q_G becomes larger, the fluorescence quantum yield decreases, meaning that for the substituents close to neutral afforded, we measured the highest values of Φ_F . This would mean that, when the *ortho*-substituent is highly charged, it favors some interactions that help to reach the TS_{rot} in non-polar solvents; and, as we have already explained, when the molecule possesses *ortho* hindrance, it favors radiative relaxation. Therefore, large values of Q_G regulate how difficult is to reach the rotational barrier and how much favored the emission properties would be. Fig. 14c shows the final trend established by Q_G , and it is possible to see that for positive values of Q_G , $\Delta\delta_F$ decreases until the most positively charged species present to BODIPY-fluorine's differentiation NO ENTIENDO ESTO. In contrast, the most negatively charged species are the ones with large $\Delta\delta_F$ values, showing that attractive or repulsive interactions are dictating the magnitude of this magnetic differentiation, as established by the value of Q_G .

Conclusions

A series of *meso*-substituted BODIPYs were synthesized. *Ortho*-aryl substitution proved to be a factor of important influence in the spectroscopic and photophysical properties. The magnitude and nature of the electrostatic interaction between *ortho*-substituents and the fluorine atoms of the BODIPY gives rise to an observable differentiation by ^{19}F -NMR, which is influenced and somewhat established by group electronegativity, hardness/softness and σ_I -Hammett constant of the *ortho* substituent. As $\Delta\delta_F$ increases, the group electronegativity and the σ -Hammett constants increases.

This kind of substitution pattern improved greatly the fluorescence quantum yield compared to the reference *meso*-phenyl-BODIPY in non-polar solvents. Computational studies on the rotational energy barriers and charge partition, provided insight on the TS_{rot} geometries and the close relationship between rotational barriers, $\Delta\delta_F$ and fluorescence quantum yields. The study of these parameters showed a structure-property relationship that provides design arguments for this kind of fluorophores.

Experimental Section

Materials and methods

Chemicals used for the synthesis were reagent grade. Spectroscopic grade solvents were used for all photophysical measurements. 1H , ^{13}C , ^{11}B and ^{19}F NMR spectra were recorded with Bruker 400 MHz, VARIAN Unity Inova 300 MHz and Anasazi 90 MHz spectrometers. Chemical shifts for 1H and ^{13}C NMR spectra are referenced relative to the residual protonated solvent. The ^{11}B NMR chemical shift is referenced relative to $BF_3 \cdot Et_2O$ ($\delta = 0$ ppm), and the ^{19}F NMR chemical shift is given relative to $CFCl_3$ ($\delta = 0$ ppm). Data are listed in parts per million

(ppm). UV-visible spectra were recorded on a VARIAN spectrometer. Fluorescence spectra were recorded on a VARIAN spectrophotometer with a slit width of 10nm, at 480 nm excitation wavelength and emission from 490 to 750 nm. The corresponding fluorescence quantum yield (Φ_f) was calculated according to a standard solution of Rhodamine 6G in ethanol and was determined using the equation below,

$$\Phi_x = \Phi_s \left(\frac{A_s}{A_x} \right) \left(\frac{F_x}{F_s} \right) \left(\frac{n_x}{n_s} \right)^2$$

Where Φ is the fluorescence quantum yield, A is the absorbance, F corresponds to the area under the emission curve and n is the refractive index of the solvents used in the measurement. The subscripts x and s represent the tested dye and the standard dye (Rhodamine), respectively.

General Synthesis

Synthesis of dipyrromethanes: To a solution of the corresponding aromatic aldehyde (1 eq.) in pyrrole (4 eq.), was added a catalytic amount of trifluoroacetic acid (TFA). The mixture was stirred at room temperature until total consumption of the aldehyde. The crude product was washed with brine, extracted with dichloromethane, dried over anhydrous Na_2SO_4 and evaporated to dryness under vacuum. This crude was then purified in column chromatography on silica gel using hexane/ethyl acetate.³⁰ CREO QUE VA SIN PUNTO

Synthesis of BODIPYs: Into the corresponding dipyrromethane dissolved in CH_2Cl_2 , DDQ (2,3-dichloro-5,6-dicyano-1,4-benzoquinone) (1 eq.) was added and the solution was stirred 1 h at room temperature. To this oxidized product, $BF_3 \cdot Et_2O$ (6 eq.) was added under nitrogen atmosphere and stirred for another 15 min, then, triethylamine (3 eq.) was added dropwise and stirring was continued to completion of the reaction and monitored by TLC. The reaction mixture was then washed with brine and extracted with CH_2Cl_2 , the organic layer was combined, dried over Na_2SO_4 and evaporated to dryness under vacuum to give the crude product. This was further purified by silica gel column chromatography to afford the corresponding BODIPY.³¹

Characterization

4,4-difluoro-8-phenyl-4-bora-3a,4a-diaza-s-indacene (1). Column chromatography using hexane/ethyl acetate (8:2) afforded **1**³² as a green crystalline solid (60%). Mp: 103 °C. 1H NMR [400 MHz, $CDCl_3$] (δ , ppm): 7.95 (m, 2H), 7.51–7.60 (m, 5H), 6.94 (d, $J = 3.6$ Hz, 2H), 6.55 (d, $J = 3.6$ Hz, 2H); ^{13}C NMR [100 MHz, $CDCl_3$] (δ , ppm): 147.3, 144.0, 134.9, 133.7, 131.6, 130.74, 130.44, 128.4. ^{11}B NMR [160 MHz, $CDCl_3$] (δ , ppm): -0.29 (t, $J_{B-F} = 29$ Hz). ^{19}F NMR [282 MHz, $CDCl_3$] (δ , ppm): -144.98 (q, $J_{B-F} = 29$ Hz).

4,4-difluoro-8-(4-methoxyphenyl)-4-bora-3a,4a-diaza-s-indacene (2). Column chromatography with hexane/ethyl acetate (8:2) afforded **2**³³ as an orange powder (61%). Mp: 120–122 °C. ¹H NMR [400 MHz, CDCl₃] (δ, ppm): 7.92 (s, 2H), 7.55 (d, *J* = 8.8 Hz, 2H), 7.05 (d, *J* = 8.9 Hz, 2H), 6.98 (d, *J* = 4 Hz, 2H), 6.56–6.54 (m, 2H), 3.92 (s, 3H). ¹³C NMR [100 MHz, CDCl₃] (δ, ppm): 162.3, 147.7, 143.6, 135.1, 132.6, 131.6, 126.6, 118.4, 114.3, 55.7. ¹¹B NMR [160 MHz, CDCl₃] (δ, ppm): -0.26 (t, *J*_{B-F} = 28 Hz). ¹⁹F NMR [282 MHz, CDCl₃] (δ, ppm): -145.19 (q, *J*_{B-F} = 28 Hz).

4,4-difluoro-8-(4-hydroxyphenyl)-4-bora-3a,4a-diaza-s-indacene (3). Column chromatography using hexane/ethyl acetate (8:2) afforded **3**³⁴ as a red crystalline solid (46%). Mp: 151 °C. ¹H NMR [400 MHz, CDCl₃] (δ, ppm): 7.95 (s, 2H), 7.50 (d, *J* = 8.6 Hz, 2H), 6.99 (m, 4H), 6.57 (d, *J* = 2.4 Hz, 2H), 5.82 (s, 1H). ¹³C NMR [100 MHz, CDCl₃] (δ, ppm): 158.6, 147.4, 143.5, 134.8, 132.6, 131.4, 126.3, 118.4, 115.6. ¹¹B NMR [160 MHz, CDCl₃] (δ, ppm): -0.25 (t, *J*_{B-F} = 28 Hz). ¹⁹F NMR [376 MHz, CDCl₃] (δ, ppm): -144.56 (q, *J*_{F-B} = 29 Hz).

4,4-difluoro-8-(2-methylphenyl)-4-bora-3a,4a-diaza-s-indacene (4). Column chromatography using hexane/ethyl acetate (8:2) afforded **4**³² as a green solid (10%). Mp: 135 °C. ¹H NMR [400 MHz, CDCl₃] (δ, ppm): 7.93 (s, 2H), 7.45–7.39 (m, 1H), 7.33 (d, *J* = 7.9 Hz, 1H), 7.30–7.23 (m, 2H), 6.71 (d, *J* = 4.1 Hz, 2H), 6.49 (d, *J* = 4.0 Hz, 2H), 2.24 (s, 3H). ¹³C NMR [100 MHz, CDCl₃] (δ, ppm): 147.2, 144.5, 136.5, 135.6, 133.1, 131.2, 130.6, 129.9, 129.8, 125.4, 118.7, 20.1. ¹¹B NMR [128 MHz, CDCl₃] (δ, ppm): 0.31 (t, *J*_{B-F} = 28 Hz). ¹⁹F NMR [376 MHz, CDCl₃] (δ, ppm): -144.87 (dq, *J*_{B-Fa} = 28 Hz, *J*_{F-F} = 104 Hz), -145.56 (dq, *J*_{B-Fb} = 28 Hz, *J*_{F-F} = 104 Hz).

4,4-difluoro-8-(2-methoxyphenyl)-4-bora-3a,4a-diaza-s-indacene (5). Column chromatography using hexane/ethyl acetate (8:2) afforded **5**³⁵ as an orange powder (20%). Mp: 110–112 °C. ¹H NMR [400 MHz, CDCl₃] (δ, ppm): 7.90 (s, 2H), 7.50 (td, *J*₁ = 8.3 Hz, *J*₂ = 1.6 Hz, 1H), 7.31 (dd, *J*₁ = 7.5 Hz, *J*₂ = 1.6 Hz, 1H), 7.08–7.03 (m, 2H), 6.80 (d, *J* = 4.0 Hz, 2H), 6.48 (d, *J* = 4.0 Hz, 2H), 3.75 (s, 3H). ¹³C NMR [100 MHz, CDCl₃] (δ, ppm): 157.2, 144.5, 143.8, 135.7, 131.6, 131.5, 131.1, 122.4, 120.1, 118.1, 111.3, 55.6. ¹¹B NMR [128 MHz, CDCl₃] (δ, ppm): 0.31 (t, *J*_{B-F} = 28 Hz). ¹⁹F NMR [376 MHz, CDCl₃] (δ, ppm): -144.47 (dq, *J*_{B-Fa} = 28 Hz, *J*_{F-F} = 104 Hz), -145.63 (dq, *J*_{B-Fb} = 28 Hz, *J*_{F-F} = 104 Hz).

4,4-difluoro-8-(2,4-dimethoxyphenyl)-4-bora-3a,4a-diaza-s-indacene (6). Column chromatography using hexane/ethyl acetate (8:2) afforded **6** as a red powder (25%). Mp: 156–157 °C. FTIR-ATR (ν, cm⁻¹): 3108, 2937, 1383, 1255, 1167, 1110, 1063, 979, 837, 780, 746, 706, 618, 582, 420. ¹H NMR [400 MHz, CDCl₃] (δ, ppm): 7.87 (s, 2H), 7.24 (d, *J* = 9 Hz, 1H), 6.83 (d, *J* = 3.6 Hz, 2H), 6.59 (d, *J* = 6.4 Hz, 2H), 6.47 (d, *J* = 3.6 Hz, 2H), 3.89 (s, 3H), 3.73 (s, 3H). ¹³C NMR [100 MHz, CDCl₃] (δ, ppm): 162.7, 158.7, 144.6, 144.3, 136.4, 132.9, 131.5, 117.9, 115.3, 104.3, 99.0, 55.6, 55.5. ¹¹B NMR [128 MHz, CDCl₃] (δ, ppm): 0.29 (t, *J*_{B-F} = 29 Hz). ¹⁹F NMR [282 MHz, CDCl₃] (δ, ppm): -144.56 (dq, *J*_{B-Fa} = 29 Hz, *J*_{F-F} = 107 Hz), -145.72 (dq, *J*_{B-Fb} = 29 Hz, *J*_{F-F} = 107 Hz).

HRMS-ESI-TOF: Experimental mass for C₁₇H₁₅BFN₂O₂ *m/z* 309.120512; calculated *m/z* 309.1211 for C₁₇H₁₅BFN₂O₂; % error: 0.361884; [M-F]⁺

4,4-difluoro-8-(2-hydroxyphenyl)-4-bora-3a,4a-diaza-s-indacene (7). Column chromatography using hexane/ethyl acetate (8:2) afforded **7**³⁶ as a green powder (10%). Mp: 134–136 °C. ¹H NMR [300 MHz, CDCl₃] (δ, ppm): 7.89 (s, 2H), 7.4 (td, *J* = 7.2 Hz, *J* = 1.7 Hz, 1H), 7.25 (dd, *J* = 7.7 Hz, *J*₂ = 1.7 Hz, 1H), 7.04–6.89 (m, 2H), 6.90 (d, *J* = 3.6 Hz, 2H), 6.49 (d, *J* = 3.9 Hz, 2H). ¹³C NMR [75 MHz, CDCl₃] (δ, ppm): 153.6, 144.8, 143.0, 135.2, 132.1, 131.6, 120.4, 120.1, 120.0, 119.0, 117.1. ¹¹B NMR [160 MHz, CDCl₃] (δ, ppm): -0.28 (t, *J*_{B-F} = 28 Hz). ¹⁹F NMR [282 MHz, CDCl₃] (δ, ppm): -143.72 (dq, *J*_{B-Fa} = 28 Hz, *J*_{F-F} = 104 Hz), -144.94 (dq, *J*_{B-Fb} = 28 Hz, *J*_{F-F} = 104 Hz).

4,4-difluoro-8-(2-chlorophenyl)-4-bora-3a,4a-diaza-s-indacene (8). Column chromatography using hexane/acetone (9:1) afforded **8** as an orange-green crystalline solid (23%). Mp: 103 °C. ¹H NMR [400 MHz, CDCl₃] (δ, ppm): 7.94 (s, 2H), 7.58–7.52 (m, 1H), 7.52–7.45 (m, 1H), 7.43–7.35 (m, 2H), 6.73 (d, *J* = 4.1 Hz, 2H), 6.51 (d, *J* = 4.1 Hz, 2H). ¹³C NMR [100 MHz, CDCl₃] (δ, ppm): 145.1, 143.5, 135.4, 133.3, 132.5, 131.6, 131.2, 131.2, 130.3, 126.6, 118.9. ¹¹B NMR [128 MHz, CDCl₃] (δ, ppm): -0.68 (t, *J* = 28 Hz). ¹⁹F [376 MHz, CDCl₃] (δ, ppm): -144.47 (dq, *J*_{B-Fa} = 28 Hz, *J*_{F-F} = 105 Hz), -145.67 (dq, *J*_{B-Fb} = 28 Hz, *J*_{F-F} = 105 Hz). ES-MS: (C₁₅H₁₀BClF₂N₂) 283.5 [M⁺ - F].

4,4-difluoro-8-(2-fluorophenyl)-4-bora-3a,4a-diaza-s-indacene (9). Column chromatography using hexane/ethyl acetate (9:1) afforded **9** as a red crystalline solid (16%). ¹H NMR [90 MHz, CDCl₃] (δ, ppm): 7.49 (s, 2H), 7.24–6.77 (m, 4H), 6.51 (d, *J* = 3.8 Hz, 2H), 6.18 (d, *J* = 4.0 Hz, 2H). ¹⁹F NMR [84.7 MHz, CDCl₃] (δ, ppm): -110.86 (s), -143.88 (dq, *J*_{B-Fa} = 28 Hz, *J*_{F-F} = 104 Hz), -145.35 (dq, *J*_{B-Fb} = 28 Hz, *J*_{F-F} = 104 Hz).

4,4-difluoro-8-(2-nitrophenyl)-4-bora-3a,4a-diaza-s-indacene (10). Column chromatography using hexane/ethyl acetate (8:2) afforded **10**²⁰ as an orange solid (14%). Mp: 198 °C. ¹H NMR [500 MHz, CDCl₃] (δ, ppm): 8.22 (dd, *J* = 7.8, 1.6 Hz, 1H), 7.95 (s, 2H), 7.84–7.69 (m, 2H), 7.57 (dd, *J* = 7.4, 1.6 Hz, 1H), 6.67 (d, *J* = 4.2 Hz, 2H), 6.51 (d, *J* = 4.3 Hz, 2H). ¹³C NMR [125 MHz, CDCl₃] (δ, ppm): 149.1, 145.3, 142.6, 134.6, 133.2, 132.3, 131.3, 129.8, 128.4, 125.2, 119.2. ¹¹B NMR [160 MHz, CDCl₃] (δ, ppm): -0.69 (t, *J* = 28 Hz). ¹⁹F [470 MHz, CDCl₃] (δ, ppm): -143.92 (dq, *J*_{B-Fa} = 28 Hz, *J*_{F-F} = 104 Hz), -146.32 (dq, *J*_{B-Fb} = 28 Hz, *J*_{F-F} = 104 Hz).

4,4-difluoro-8-(1-pyrene)-4-bora-3a,4a-diaza-s-indacene (11). Column chromatography using hexane/ethyl acetate (9:1) afforded **11**¹⁷ as a green crystalline powder (20% yield). Mp: 134–135 °C. ¹H NMR [400 MHz, CDCl₃] (δ, ppm): 8.3–8.0 (m, 11H), 6.62 (d, *J* = 4.2 Hz, 2H), 6.46 (d, *J* = 3.0 Hz, 2H). ¹³C NMR [100 MHz, CDCl₃] (δ, ppm): 146.6, 144.5, 136.6, 132.6, 131.8, 131.4, 130.8, 130.5, 129.1, 128.6, 127.9, 127.9, 127.2, 126.7, 126.3, 126.0, 125.0, 124.6, 124.3, 124.1, 118.9. ¹¹B NMR [160 MHz, CDCl₃] (δ, ppm): -0.06 (t, *J*_{B-F} = 28 Hz). ¹⁹F NMR [282 MHz,

CDCl_3] (δ , ppm): -144.51 (dq, $J_{\text{B-Fa}} = 28$ Hz, $J_{\text{F-F}} = 104$ Hz), -145.26 (dq, $J_{\text{B-Fb}} = 28$ Hz, $J_{\text{F-F}} = 104$ Hz).

Computational Methodology

All calculations were carried out taking hexane as solvent, trying to match or correlate experimental observations in a solvent with good emission properties and discarding toluene to avoid possible π -stacking interactions with the studied species.

Geometry optimizations were carried out through all-electron calculations using the B3LYP hybrid functional at the def2SVP theory level using the SMD solvation approach, to obtain the geometries of lowest energy for the studied species and to analyze important structural details.

Regarding the computation of rotational barriers, all geometries were re-optimized with the M06-2X hybrid functional and the def2SVP basis set using the SMD solvation model to refine the computation of energetics. Scans through redundant coordinates for the dihedral angle between the BODIPY and the *meso* substituents were done using M06-2X/def2SVP approach with the SMD solvation model. Being this combination a proven approach in the field of thermochemistry, energetics, energy barriers, among other features.^{37–39}

The energy maximum of each corresponding scan was then optimized as a transition state (TS) to determine the real geometry and rotational barrier of such TSs. This was done also with the M06-2X/def2SVP theory level and SMD solvation approach. Time-dependent Density Functional Theory (TD-DFT) calculations were run using the same functional at the 6-311g(d,p) theory level with the CPCM solvation method, to obtain the value for the dipole moment corresponding to the main transition ($S_0 \rightarrow S_1$) for all BODIPY derivatives.

After determining the orbital behavior of the $S_0 \rightarrow S_1$ transition, the energetic evolution of S_1 was calculated at the M06-2X/def2SVP theory level using the SMD solvation method in hexane, by TDDFT approach to the most representative points in the rotational scan. The vertical transition energies would shape the curve for the energy of the S_1 excited state for each species, as a function of dihedral angle, to be compared to the rotational energy barriers. Which is an approach known in the literature to describe similar phenomena to the one studied in the out contribution.⁴⁰

Natural Population Analysis (NPA) was performed for all compounds using the B3LYP functional at the 6-31g(d,p) theory level to calculate the charge partition for all atoms in the studied species and thus, calculate hardness/softness of the functional groups in the aryl portions of the BODIPY derivatives. Electrostatic potential (ESP) maps as surfaces and contours were produced to analyze the distribution of electrostatic partition in all the studied molecules, these computations were done using the CPCM solvation model.

All calculations were run using the Gaussian 09 software and the GaussView 5.0 visualization suite.⁴¹

Conflicts of interest

There are no conflicts to declare.

Acknowledgements

MFP (576515) and OGA (239984) thank CONACYT for their doctoral scholarship. The authors ~~Th~~ would acknowledge financial support from ~~to~~ CONACYT, PAIP and PAPIIP IN222819 DGAPA and the French-Mexican International Laboratory (LIA-LCMMC-CONACYT). Thanks to María Luisa Rodríguez, María Eugenia Ochoa for NMR experiments and Geiser Cuellar for Mass Spectra.

Notes and References

1. Treibs A, Kreuzer F-H. Difluoroboryl-Komplexe von Di- und Tripyrrylmethenen. *Justus Liebig's Ann Chem.* 1968;718(1):208-223.
2. Lakshmi V, Lee W-Z, Ravikanth M. Synthesis, structure and spectral and electrochemical properties of 3-pyrrolyl BODIPY-metal dipyrin complexes. *Dalt Trans.* 2014;43(42):16006-16014. doi:10.1039/C4DT01970A
3. Loudet A, Burgess K. BODIPY Dyes and Their Derivatives : Syntheses and Spectroscopic Properties. *Chem Rev.* 2007;107(11):4891-4932. doi:10.1021/cr078381n
4. Kálai T, Hideg K. Synthesis of new, BODIPY-based sensors and labels. *Tetrahedron.* 2006;62(44):10352-10360. doi:10.1016/j.tet.2006.08.079
5. Choi S, Bouffard J, Kim Y. Aggregation-induced emission enhancement of a meso-trifluoromethyl BODIPY via J-aggregation. *Chem Sci.* 2014;5(2):751-755. doi:10.1039/C3SC52495G
6. Guo H, Jing Y, Yuan X, et al. Highly selective fluorescent OFF-ON thiol probes based on dyads of BODIPY and potent intramolecular electron sink 2,4-dinitrobenzenesulfonyl subunits. *Org Biomol Chem.* 2011;9(10):3844-3853. doi:10.1039/c0ob00910e
7. Bura T, Retailleau P, Ulrich G, Ziessel R. Highly substituted Bodipy dyes with spectroscopic features sensitive to the environment. *J Org Chem.* 2011;76(4):1109-1117. doi:10.1021/jo102203f
8. Xochitlotzi-Flores E, Islas-Mejía AA, García-Ortega H, et al. On the structure of meso-substituted F-BODIPYs and their assembly in molecular crystals: An experimental-theoretical approach. *J Organomet Chem.* 2016;805:148-157. doi:10.1016/j.jorganchem.2016.01.021
9. Singh SP, Gayathri T. Evolution of BODIPY Dyes as Potential Sensitizers for Dye-Sensitized Solar Cells. *European J Org Chem.* 2014;2014(22):4689-4707. doi:10.1002/ejoc.201400093
10. Ozdemir M, Choi D, Kwon G, et al. Solution-Processable BODIPY-Based Small Molecules for Semiconducting Microfibers in Organic Thin-Film Transistors. *ACS Appl Mater Interfaces.* 2016;8(22):14077-14087. doi:10.1021/acsami.6b02788
11. Dale CL, Hill SJ, Kellam B. New potent, short-linker BODIPY-

- 630/650TM labelled fluorescent adenosine receptor agonists. *Med Chem Commun.* 2012;3:333-338. doi:10.1039/c2md00247g
12. Xochitiotzi-Flores E, Jiménez-Sánchez A, García-Ortega H, et al. Optical properties of two fluorene derived BODIPY molecular rotors as fluorescent ratiometric viscosity probes. *New J Chem.* 2016;40(5):4500-4512. doi:10.1039/C5NJ03339J
 13. Awuah SG, You Y. Boron dipyrromethene (BODIPY)-based photosensitizers for photodynamic therapy. *RSC Adv.* 2012;2(30):11169. doi:10.1039/c2ra21404k
 14. Zissel R, Ulrich G, Harriman A. The chemistry of Bodipy: A new El Dorado for fluorescence tools. *New J Chem.* 2007;31(4):496-501. doi:10.1039/b617972j
 15. Tram K, Yan H, Jenkins H a., Vassiliev S, Bruce D. The synthesis and crystal structure of unsubstituted 4,4-difluoro-4-bora-3a,4a-diaza-s-indacene (BODIPY). *Dye Pigment.* 2009;82(3):392-395. doi:10.1016/j.dyepig.2009.03.001
 16. Merkushev DA, Usoltsev SD, Marfin YS, et al. BODIPY associates in organic matrices: Spectral properties, photostability and evaluation as OLED emitters. *Mater Chem Phys.* 2017;187:104-111. doi:10.1016/j.matchemphys.2016.11.053
 17. Bañuelos J, Arroyo-Córdoba JJ, Valois-Escamilla I, et al. Modulation of the photophysical properties of BODIPY dyes by substitution at their meso position. *RSC Adv.* 2011;1(4):677-684. doi:10.1039/c1ra00020a
 18. Benniston AC, Harriman A, Whittle VL, Zelzer M. Molecular rotors based on the boron dipyrromethene fluorophore. *European J Org Chem.* 2010;(3):523-530. doi:10.1002/ejoc.200901135
 19. Hermanek S. "B NMR Spectra of Boranes, Main-Group Heteroboranes, and Substituted Derivatives. Factors Influencing Chemical Shifts of Skeletal Atoms. *Chem Rev.* 1992;92:352-362. doi:10.1021/cr00010a007
 20. Doulain P-E, Goze C, Bodio E, Richard P, Decréau RA. BODIPY atropisomer interconversion, face discrimination, and superstructure appending. *Chem Commun (Camb).* 2016;52(24):4474-4477. doi:10.1039/c5cc10526a
 21. Kubin RF, Fletcher AN. Fluorescence quantum yields of some rhodamine dyes. *J Lumin.* 1982. doi:10.1016/0022-2313(82)90045-X
 22. Collado-Fregoso E, Zugazagoitia JS, Plaza-Medina EF, Peon J. Excited-state dynamics of nitrated push-pull molecules: The importance of the relative energy of the singlet and triplet manifolds. *J Phys Chem A.* 2009;113(48):13498-13508. doi:10.1021/jp905379y
 23. Ulrich G, Zissel R, Harriman A. The chemistry of fluorescent bodipy dyes: versatility unsurpassed. *Angew Chem Int Ed Engl.* 2008;47(7):1184-1201. doi:10.1002/anie.200702070
 24. Winnik F. Photophysics of Preassociated Pyrenes in Aqueous Polymer Solutions and in Other Organized Media. *Chem Rev.* 1993;93(2):587-614. doi:10.1021/cr00018a001
 25. Niko Y, Sasaki S, Narushima K, Sharma DK, Vacha M, Konishi GI. 1-, 3-, 6-, and 8-Tetrasubstituted Asymmetric Pyrene Derivatives with Electron Donors and Acceptors: High Photostability and Regioisomer-Specific Photophysical Properties. *J Org Chem.* 2015;80(21):10794-10805. doi:10.1021/acs.joc.5b01987
 26. Kee HL, Kirmaier C, Yu L, et al. Structural control of the photodynamics of boron-dipyrin complexes. *J Phys Chem B.* 2005;109(43):20433-20443. doi:10.1021/jp0525078
 27. De Proft F, Langenaeker W, Geerlings P. Ab initio determination of substituent constants in a density functional theory formalism: Calculation of intrinsic group electronegativity, hardness, and softness. *J Phys Chem.* 1993;97(9):1826-1831. doi:10.1021/j100111a018
 28. Takahata Y, Chong DP. Estimation of Hammett sigma constants of substituted benzenes through accurate density-functional calculation of core-electron binding energy shifts. *Int J Quantum Chem.* 2005;103(5):509-515. doi:10.1002/qua.20533
 29. Kaya S, Kaya C. A new equation for calculation of chemical hardness of groups and molecules. *Mol Phys.* 2015;113(11):1311-1319. doi:10.1080/00268976.2014.991771
 30. Gryko DT, Gryko D, Lee C-H. 5-Substituted dipyrans: synthesis and reactivity. *Chem Soc Rev.* 2012;41(10):3780-3789. doi:10.1039/c2cs00003b
 31. Wagner RW, Lindsey JS. Boron-dipyrromethene dyes for incorporation in synthetic multi-pigment light-harvesting arrays. *Pure Appl Chem.* 1996;68(7):1373-1380. doi:10.1351/pac199668071373
 32. Kee HL, Kirmaier C, Yu L, et al. Structural Control of the Photodynamics of Boron - Dipyrin Complexes. *J Phys Chem B.* 2005;109:20433-20443. doi:10.1021/jp0525078
 33. Betancourt-Mendiola L, Valois-Escamilla I, Arbeloa T, et al. Scope and Limitations of the Liebeskind-Srogl Cross-Coupling Reactions Involving the Biellmann BODIPY. *J Org Chem.* 2015;80(11):5771-5782. doi:10.1021/acs.joc.5b00731
 34. Baruah M, Qin W, Basarić N, De Borggraeve WM, Boens N. BODIPY-based hydroxyaryl derivatives as fluorescent pH probes. *J Org Chem.* 2005;70(10):4152-4157. doi:10.1021/jo0503714
 35. Roacho RI, Metta-Magaña AJ, Peña-Cabrera E, Pannell KH. Synthesis, structural characterization, and spectroscopic properties of the ortho, meta, and para isomers of 8-(HOCH₂-C₆H₄)-BODIPY and 8-(MeOC₆H₄)-BODIPY. *J Phys Org Chem.* 2013;26(4):345-351. doi:10.1002/poc.3095
 36. Kim T-I, Maity SB, Bouffard J, Kim Y. Molecular Rotors for the Detection of Chemical Warfare Agent Simulants. *Anal Chem.* 2016;88:9259-9263. doi:10.1021/acs.analchem.6b02516
 37. Mardirossian N, Head-Gordon M. How Accurate Are the Minnesota Density Functionals for Noncovalent Interactions, Isomerization Energies, Thermochemistry, and Barrier Heights Involving Molecules Composed of Main-Group Elements? *J Chem Theory Comput.* 2016;12(9):4303-4325. doi:10.1021/acs.jctc.6b00637
 38. Weigend F, Ahlrichs R. Balanced basis sets of split valence, triple zeta valence and quadruple zeta valence quality for H

- to Rn: Design and assessment of accuracy. *Phys Chem Chem Phys*. 2005;7(18):3297-3305. doi:10.1039/b508541a
39. Marenich A V., Cramer CJ, Truhlar DG. Universal solvation model based on solute electron density and on a continuum model of the solvent defined by the bulk dielectric constant and atomic surface tensions. *J Phys Chem B*. 2009;113(18):6378-6396. doi:10.1021/jp810292n
40. Kubli-Garfias C, Salazar-Salinas K, Perez-Angel EC, Seminario JM. Light activation of the isomerization and deprotonation of the protonated Schiff base retinal. *J Mol Model*. 2011;17(10):2539-2547. doi:10.1007/s00894-010-0927-x
41. Frisch MJ, Trucks GW, Schlegel HB, et al. Gaussian 09, Revisions, A.02, Revision D.01, Gaussian, Inc., Wallingford, CT. 2009. <https://gaussian.com/g09citation/>. Accessed May 21, 2020.